A new analytical method for stability analysis of rock blocks with basal erosion in sub-horizontal strata by considering the eccentricity effect

Xushan Shi[1], Bo Chai[1,3,4], Juan Du[1,2,4], Wei Wang[1,3,4], Bo Liu[1]

[1]School of Environmental Studies, China University of Geosciences, Wuhan, 430078, China
[2]Centre for severe weather and climate and hydrogeological hazards, Wuhan, 430078, China
[3]Hubei Key Laboratory of Yangtze Catchment Environmental Aquatic Science, Wuhan, 430078, China
[4]Research Center for Geohazards Monitoring and Warning in Three Gorges Reservoir, Wanzhou, 404000, China

Correspondence to: Bo Chai (chaibo@cug.edu.cn) and Juan Du (dujuan@cug.edu.cn)

Abstract. The basal cavity of a rock block formed due to differential weathering is an important predisposing factor for rockfall in hard-soft interbedded rocks, which induces eccentricity situation at the base of the rock block. Rock block falling due to the non-uniform distribution with the failure modes of toppling or sliding is defined as biased rockfall in this study. Taking into account the non-uniform stress distribution due to the eccentricity effect, a new analytical method is proposed for three-dimensional stability analysis of biased rockfall. The development of non-uniform stress distribution stress calculated by this analytical method was verified by numerical simulation. The biased rockfall progresses from partial damage of the soft underlying layer, caused by non-uniform distributed stress, to toppling and sliding of overhanging hard rock block due to overall unbalanced force. Therefore, a set of factors of safety (Fos) against partial damage (compressive and tensile damage of the soft underlying layer) and overall failure (toppling and sliding of the hard rock block) are used to determine the rockfall susceptibility level. The analytical method is applied and validated using biased rockfalls on the northeast edge of the Sichuan Basin in Southwest China, where a significant number of rockfalls consisting of overhanging thick sandstone and underlying mudstone occur. The evolution process of biased rockfalls is divided into four stages, initial state, basal cavity formation, partial unstable and failure. The proposed method is validated by calculating Fos of the typical unstable rock blocks in the study area. As the cavity continues to grow, the continuous retreat of mudstone causes stress redistribution between the hard and soft rock layers. This results in damage to the underlying soft rock layer due to the development of the non-uniform distribution, ultimately leading to the failure of the hard rock block. The critical retreat ratio is determined to be 0.33, which is used to classify the low and moderate rockfall susceptibility in the eastern Sichuan Basin. The proposed analytical method provides insights into the evolution of biased rockfall and a means for early identification and susceptibility assessment of rockfall.

List of symbols

a length of the block along the x direction

A area of contact surfaces

32	b	width of the block along the y direction
33	c	cohesive force of the mudstone
34	d_i	width of the basal cavity in a certain direction
35	e_x	eccentric distance along the x direction
36	e_y	eccentric distance along the y direction
37	E_x	horizontal seismic force along the x direction
38	Fos	factor of safety
39	h	height of the block
40	h_w	height of the water in the fracture
41	H_x	water pressure along the x direction
42	I_x	moment of inertia with respect to the x-axis
43	I_y	moment of inertia with respect to the y-axis
44	k_e	earthquake contribution coefficient
45	k_1	rainfall coefficient, taking 1 in the rainfall scenario and 0 in the non-rainfall scenario
46	k_2	earthquake coefficient, taking 1 in the seismic scenario and 0 in the non-seismic scenario
47	k_3	free surface coefficient, taking 1 for two free surfaces and 0 for three free surfaces
48	M_{bx}	total bending moments with respect to the x-axis on the mudstone foundation
49	M_{by}	total bending moments with respect to the y-axis on the mudstone foundation
50	M_{bEx}	bending moment of E_x with respect to the x-axis on the mudstone foundation
51	M_{bHx}	bending moment of H_x with respect to the x-axis on the mudstone foundation
52	M_{bWx}	bending moment of W with respect to the x-axis on the mudstone foundation
53	M_{Ex}	overturning moment provided by E_x along the x direction
54	M_{Hx}	overturning moment provided by H_x along the x direction
55	M_{px}	stabilizing moment of p_n along the x direction
56	$M_{W_{inx}}$	stabilizing moment provided by W along the x direction
57	$M_{W_{outx}}$	overturning moment provided by W along the x direction
58	N_z	total applied vertical load on the mudstone base
59	O	origin of the (x, y) coordinates
60	$p(x, y)$	pressure magnitude at point (x, y)
61	r_i	the basal mudstone retreat ratio equal to the ratio of basal cavity width to block width in a certain direction
62	W	weight of the block
63	x	distance to O along the x-axis
64	y	distance to O along the y-axis

65	α	true dip of the contact surface
66	γ_s	unit weight of sandstone
67	γ_w	unit weight of water
68	θ_1	apparent dip of α on plane J1
69	θ_2	apparent dip of α on plane J2
70	σ_{cmax}	ultimate compressive strength of the mudstone
71	σ_{tmax}	ultimate tensile strength of the mudstone
72	τ_{max}	ultimate shear strength of the mudstone
73	φ	friction angle of the mudstone
74	ω_1	angle between the trend of the contact surface and the x direction
75	ω_2	angle between the trend of the contact surface and the y direction

1 Introduction

Rockfall is defined as the detachment of a rock block from a steep slope along a surface, on which little or no shear displacement takes place (Cruden and Varnes, 1996). Rockfalls frequently occur in mountainous ranges, cut slopes, and coastal cliffs, and they may cause significant facility damage and casualties in residential areas and transport corridors (Chau et al., 2003; Volkwein et al., 2011; Corominas et al., 2018). Stability analysis of rock blocks are crucial for risk management and early warning of rockfall (Kromer et al., 2017).

Rockfalls are prone to occur in soft-hard rock formations, and the non-uniform stress distribution caused by differential weathering of rock formations is the main reason for the failure of rockfall. In the eastern Sichuan Basin, Southwest China, rockfall is widespread and poses high risk (Chen et al., 2008; Chen and Tang, 2010; Zhang et al., 2016; Zhou et al., 2017; Zhou et al., 2018). The rockfall in this area is attributed to the tectonic setting of Jura-type folds and the stratum sequence, which is characterized by the interbedding of hard and soft layers. An alternation of thick sandstone and thin mudstone layers is formed in the wide and gentle-angle synclines (Zhang et al., 2015; Wu et al., 2018). Weathering is known to be one of the main predisposing factors for rockfall (Jaboyedoff et al., 2021; Zhan et al., 2022). The cliff comprised of hard sandstone is the source of rockfall, and the underlying mudstone is more susceptible to weathering. Along with the retreat of basal cavities in the mudstone layer, the gravity centre of the overhanging sandstone block moves outward relative to the mudstone. In this case, the stress distribution in the contact surface of sandstone and mudstone is non-uniform. The mudstone on the outer side bears higher compressive stress than that on the inner side. This phenomenon can be defined as an eccentricity effect, which leads to mudstone damage and failure of the overhanging sandstone by toppling or sliding. This type of rockfall is defined as biased rockfall in this study (Fig. 1). Similar rockfall patterns have been widely reported in other regions, such as Joss Bay in England (Hutchinson, 1972), Okinawa Island in Japan (Kogure et al., 2006), and the Colorado Plateau of the southwestern United States (Ward et al., 2011). Retreat of the basal cavity is a main cause for the failure of the overhanging block. Therefore,

97 it is necessary to establish an analytical method, considering the development of the basal cavity, to analyse the stress
98 distribution and stability of rock blocks, which is fundamental to the susceptibility assessment and risk control of biased
99 rockfall.
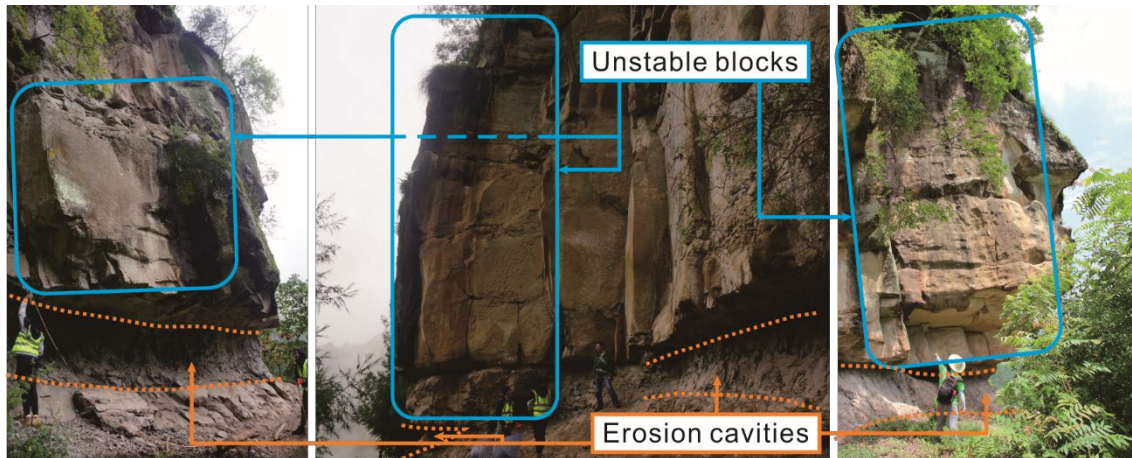
101 **Figure 1** Potential unstable blocks and basal cavities caused by differential weathering.

103 Rockfall stability analysis methods include statistical analysis (Frattini et al., 2008; Santi et al., 2009), empirical rating systems
104 (Pierson et al., 1990; Ferrari et al., 2016), and mechanical analysis (Lin and Fairhurst, 1988; Jaboyedoff et al., 2004; Derron
105 et al., 2005; Matasci et al., 2018). The statistical analysis and empirical rating systems are suitable for rockfall hazard
106 assessment at a regional scale. The accuracy of statistical analysis depends on the completeness of rockfall inventories (Chau
107 et al., 2003; Guzzetti et al., 2003; D'amato et al., 2016). However, its application to rockfall hazards is limited due to the lack
108 of complete inventory data (Budetta and Nappi, 2013; Malamud et al., 2004). Empirical and semi-empirical rating systems are
109 used where site-specific rockfall inventories are either unavailable or unreliable. Therefore, rockfall susceptibility can be
110 assessed by heuristic ranking of selected predisposing factors (Frattini et al., 2008; Budetta, 2004). Mechanical analysis based
111 on static equilibrium theory is the main method to analyse the stability of site-specific rockfall using the factor of safety (Fos).
112 Ashby (1971) conducted stability analysis with a parallelepiped block resting on an inclined plane (Fig. 2a), and the solution
113 was subsequently modified by Bray and Goodman (1981) and Sagaseta (1986). Kogure et al. (2006) utilized a cantilever beam
114 model to determine the critical state of limestone cliffs. Frayssines and Hantz (2009) proposed the limit equilibrium method
115 (LEM) to predict block stability against sliding and toppling in steep limestone cliffs (Fig. 2c). Chen and Tang (2010)
116 established a stability analysis method of three types of unstable rocks in the Three Gorges Reservoir area with the LEM.
117 Alejano et al. (2015) studied the influence of rounding of block corners on the block stability. Zhang et al. (2016) defined Fos
118 based on fracture mechanics and studied the progressive failure process by analysing crack propagation. Alejano et al. (2010)
119 and Pérez-Rey et al. (2021) deduced a formula for Fos of blocks with more complex geometry.
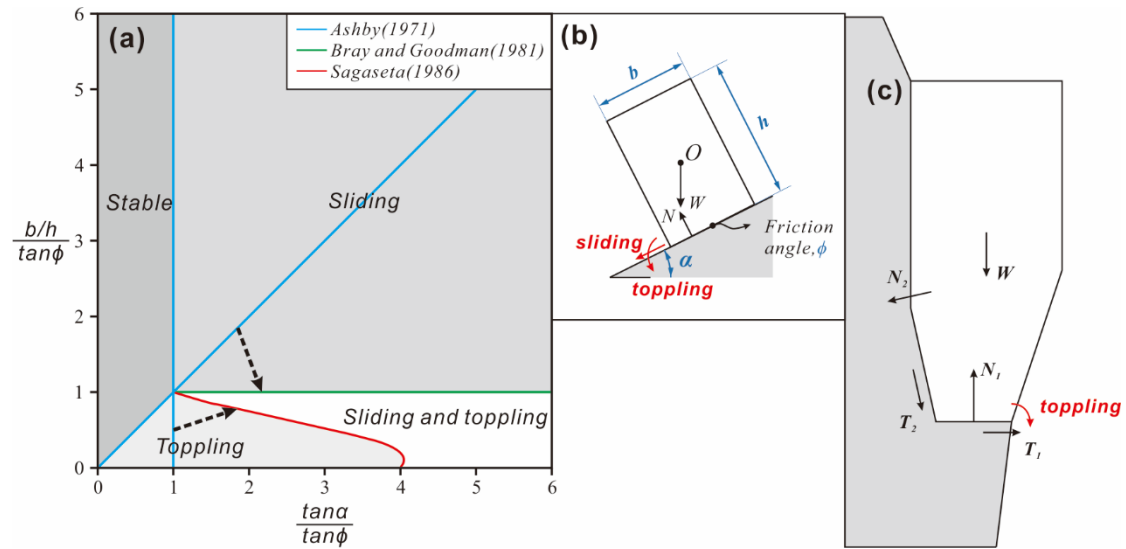
Figure 2 Traditional force analysis diagrams of the rock block. (a) and (b) are stability analysis diagrams of rock blocks under dynamic conditions, resting on an inclined plane with a dip angle of α. The rock block is generalized as a cuboid with dimensions $b \times h$ and weight W (as modified from Ashby (1971), Bray and Goodman (1981) and Sagaseta (1986)). (c) Force description of the toppling model proposed by Frayssines and Hantz (2009). In the above assumptions, N, T, and W are regarded as forces applied at a point.

The supporting force on the contact surface is assumed to be applied at a point in the current LEM methods (i.e., N in Fig. 2 b and c). However, the supporting force is actually a distributed force. The external erosion generates an eccentricity situation on the overhanging rock block and results in a non-uniform distribution of the supporting force on the contact surface, which is not considered in the traditional LEM. The presence of non-uniform stress distribution plays a critical role in inducing localized damage within a rock mass. Damage is frequently considered as an indicator or a threshold for the onset of accelerated failure in rock masses (Zhang et al., 2016). Therefore, it is imperative to consider the non-uniform stress distribution for the rockfall stability analysis. Furthermore, most studies simplified the three-dimensional geometry of the rock block by one cross-section, which is used to represent the critical features of the slope structure. Nevertheless, for natural blocks with basal cavities, the cavities usually present different depths along different directions (Pérez-Rey et al., 2021). Therefore, a three-dimensional model is necessary to accurately calculate the stability. In addition, when a block has multiple free faces and a complex structure, its potential failure is dominated by different modes, including rock mass damage and overall block failure. Therefore, the probable failure modes should be determined prior to the calculation of Fos.

Based on rockfall investigation in the Eastern Sichuan Basin, China, the main objective of this study was to propose a new three-dimensional method for the determination of failure modes and Fos of biased rockfall, considering the non-uniform force distribution on the contact surfaces. Compared with the traditional LEM method, this study takes into account the partial damage of the underlying soft rock and the overall instability of the overhanging hard rock blocks, and can evaluate the stability of biased rockfall more comprehensively. Fos of the typical unstable rock blocks in the study area are calculated to validate

143 the proposed method. In addition, the critical mudstone retreat ratio in this area is analysed. This study is an extension of the
144 basic LEM for rockfall, which can promote the accuracy of rockfall stability analysis and facilitate rockfall prevention and
145 risk mitigation.

146 **2 Study area**

147 **2.1 Geological setting**

148 The study area is located on the northeastern edge of the Sichuan Basin, China (Fig. 3a). Continuous erosion processes generate
149 moderate-low mountain and valley landforms (Yu et al., 2021). The tectonic structure of this area is characterized by a series
150 of ENE anticlines and synclines (Fig. 3b, c). In the anticline area, the rock layers dip relatively steeply, where translational
151 rockslides are the main mode of slope failure. The syncline area is dominated by gently dipping strata and is prone to rockfall
152 (Zhou et al., 2018). The study area is located in the core of the Matouchang syncline, where the rock layers are sub-horizontal
153 (Fig. 3d, e). In this valley, due to the longstanding fluvial incision, the relative relief is approximately 500 m and the valley
154 flanks are extremely steep (Fig. 3e). In addition, the toes of the hill slopes are reshaped because of the construction of the
155 G318 national road, which is the main traffic line and is always threatened by rockfalls from steep rock slopes (shown in Fig.
156 3d and Table 1).
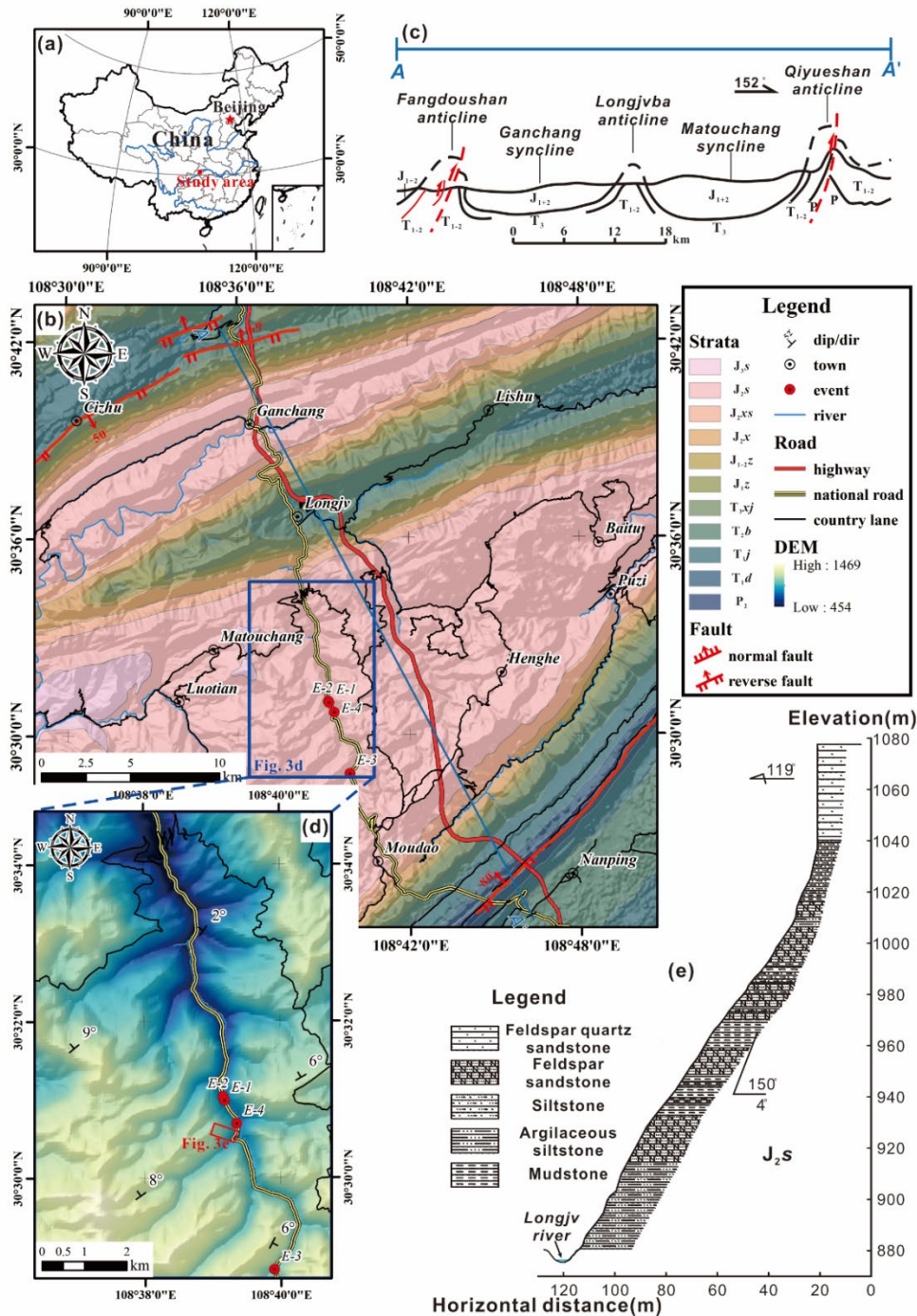
157

158 **Figure 3** (a) Location of the study area in China; (b) geological map of the study area; (c) tectonic sketch profile of A-A', whose location is

159 showed in Fig. 3b; (d) rockfall-prone segment and key investigation areas. The red dots are the positions of historical rockfall events,

160 corresponding to the numbers in Table 1; (e) Geological cross-section of the hillslope in the Jitougou section of G318 national road, which

161 is marked by a red rectangle in Fig. 3d.

Table 1 Historical rockfall events along G318 national road in the study area

No	Location	Time of occurrence (GMT+8)	Volume [m³]	Consequence
E-1	K1698+900	2014-05 to 06*	Unknown	The power transmission facilities outside the road were smashed.
E-2	K1699+000	2015-02-14 23:00	About 240	A passing truck was stuck and two people dead.
E-3	K1690+700	2015-06-16	Unknown	The road was interrupted for a day.
E-4	K1698+400	2015-06-18 09:00	About 200	A vehicle was crashed into a gully and four people dead.

163 *Note: The exact time is unknown.
164

2.2 Rockfall characteristics

The slopes in the study area consist of a sub-horizontally interbedded sandstone and mudstone layer. Therefore, there are multiple layers of potentially unstable rock blocks in the hill slopes (Fig 4a). The thick sandstone has two sets of sub-vertical joints (Fig. 5), which cut the rock mass into blocks as the potential rockfall source (Fig. 4b). Basal cavities have formed in the underlying mudstone layer (Fig. 4c, d). Joints and bedding planes (BP) constitute the detachment surfaces between the blocks and steep slope (Fig. 4e). The eccentricity effect produced by the mudstone external erosion plays an important role in the evolution process of rockfall. When the basal mudstone cannot provide adequate supporting force, the blocks detach from the steep slope, and biased rockfall occurs. Sliding and toppling are two possible failure modes of biased rockfall.
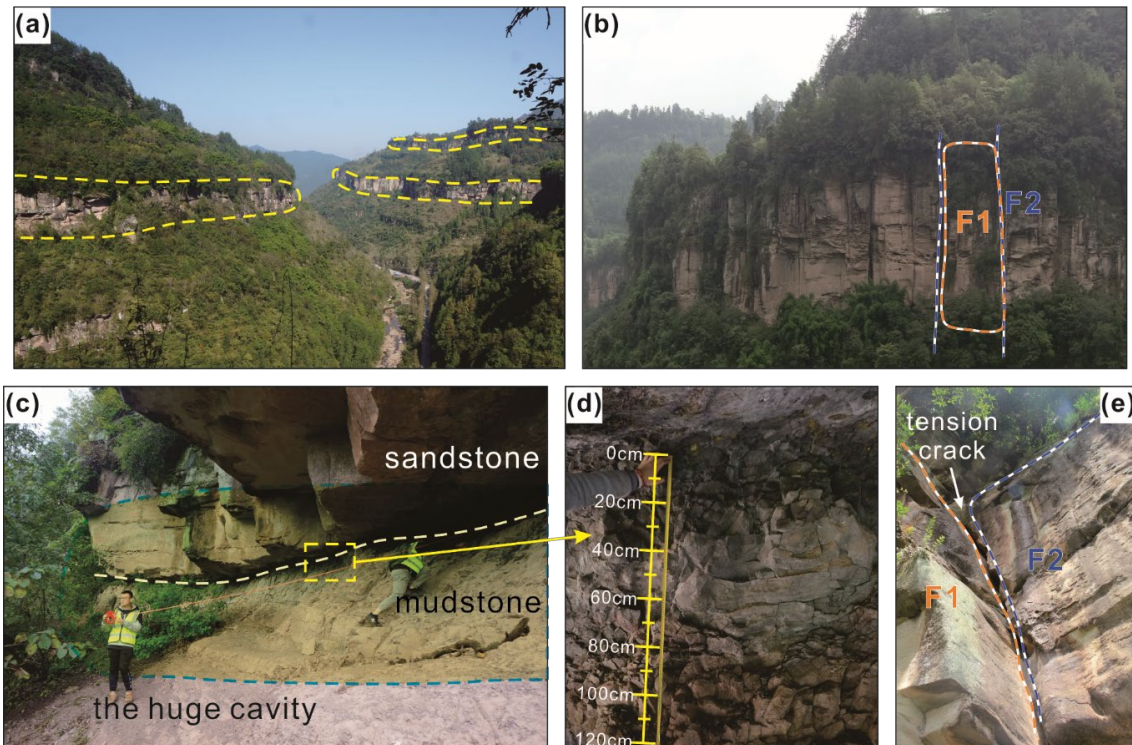
Figure 4 Characteristics of biased rockfalls in the study area. (a) Multiple-layers of rockfall sources, which is consist of thick sandstone. (b) Two sets of sub-vertical joints (F1 and F2) recognized by the UAV photos. (c) Large basal cavity developed in the underlying mudstone. (d)

Dense fractures on the mudstone surface generated by weathering and compression. (e) Vertical tension crack in the rear of the block, through which precipitation can infiltrate.

According to the historical rockfall events in this area, precipitation is considered a triggering factor of rock instability. The precipitation mainly infiltrates along the sub-vertical joints or cracks of the sandstone (Fig. 4e). However, the drainage of fissure water is hysteretic due to the obstruction of basal mudstone. Therefore, transient steady flow exists in vertical cracks during heavy rainfall, and the hydrostatic pressure triggers the detachment of rock blocks. Thus, typical scenarios (such as rainfall intensity and earthquake) need to be considered in the stability analysis model.
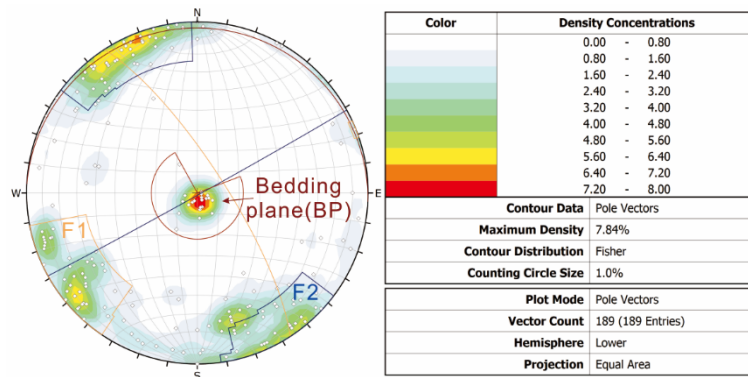
Figure 5 Stereo net produced using compass-clinometer survey data, which shows the densities and orientations of five clusters. The data were collected in the rockfall-prone area shown in Fig. 3d.

3 Calculation method

3.1 Geological models and assumptions

A detailed geological investigation of unstable rock blocks was carried out in the study area (Fig. 6). The geological model of the rock block is mainly composed of the overhanging sandstone and the underlying mudstone. The sandstone block is assumed to be a rigid body, which is divided by two sets of orthogonal vertical smooth joints without friction resistance. According to the relatively persistent sub-vertical fractures observed in the field, the vertical joints are assumed to be fully persistent in the geological model. The sandstone block is assumed to be a complete body without persistent discontinuity, and it will not disintegrate before it falls. Due to the basal cavity in mudstone, the contact surface between sandstone and mudstone exhibits an eccentricity situation where non-uniform stresses are distributed at different positions. Mudstone is mainly loaded by compressive stress and tensile stress. When the compressive stress of mudstone exceeds its strength on the outer side, some initial damage appears. The effective contact surface between mudstone and sandstone is reduced, which aggravates the non-uniform distribution of stress. In this way, the ability of mudstone to resist the sliding and toppling of overhanging sandstone is reduced. In the field, compression deformation of mudstone can be observed, which usually manifests as micro-fractures and cleavages (Fig. 4d). The deformation is very slight and slow in the short term. In addition, the LEM is essentially a

201 force/stress approach that does not take into account the deformation. Therefore, in this study, it is assumed that the mudstone
202 is not subjected to deformation. The rock block remains in the state of static equilibrium prior to the final overall failure. Fig.
203 7 displays the four evolution stages of biased rockfall. In the initial stage, the base cavity has not yet formed, and the normal
204 force acting on the contact surface is uniform in different positions. The eccentricity effect leads to a non-uniform supporting
205 force as the basal cavity grows, and partial damage gradually develops when the non-uniform stress exceeds the compressive
206 or tensile strength of the mudstone. Under the triggering effects of rainfall or earthquakes, the rock blocks are separated by
207 sliding or toppling.
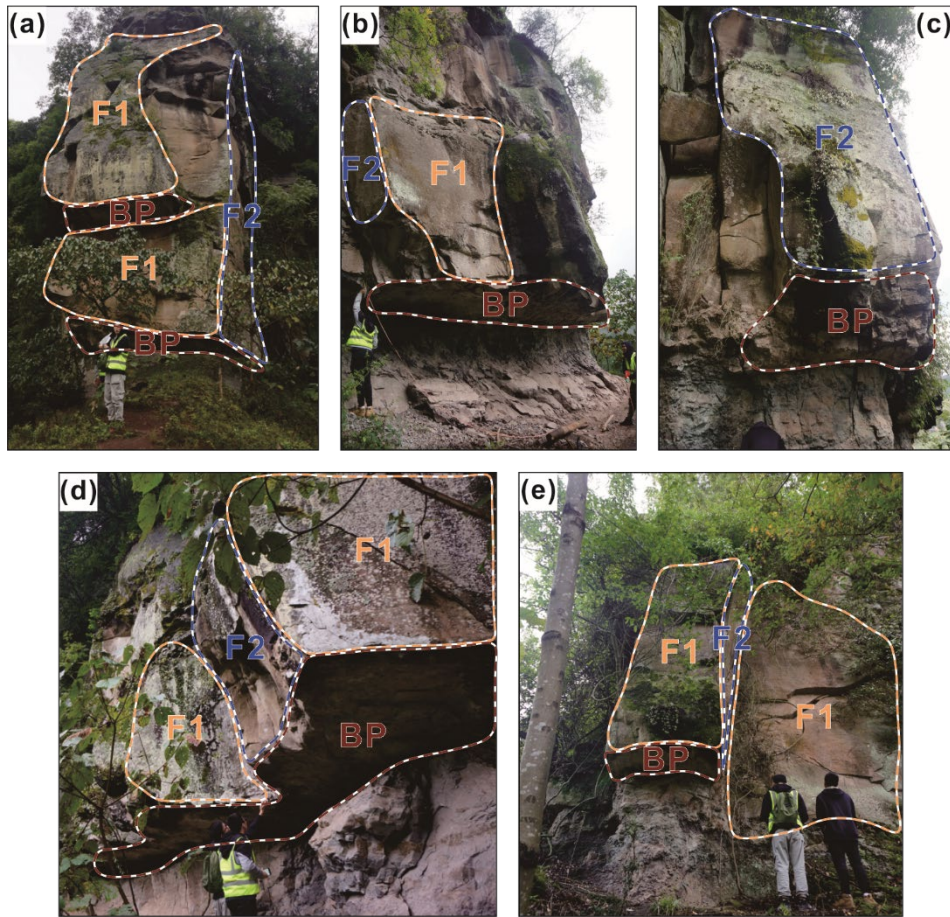
208
209 **Figure 6** The unstable blocks were labelled W02, W08, W18, W04, and W21, which are detached by the dominating discontinuities in Fig.
210 5. Basal cavities can be identified under the bedding planes of sandstone.
211
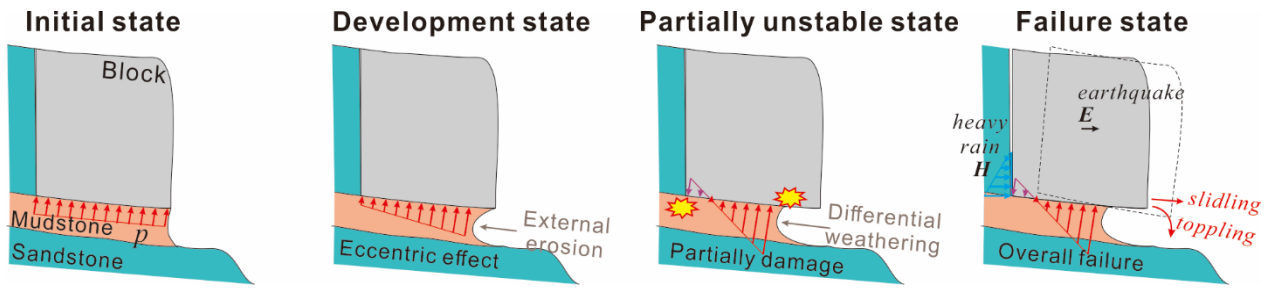
212

213 **Figure 7** The evolution process of rock blocks from stable state to failure.

214

215 Fig. 8 represents the mechanical model of the force equilibrium analysis of a rock block with two or three free faces. The rock
216 block (the overhanging sandstone) is generalized as a parallelepiped block. The underlying mudstone is impermeable, so
217 rainfall can fill the joints and transmit horizontal hydrostatic pressure. The shear strength of the underlying mudstone is
218 assumed to obey the Mohr–Coulomb criterion. Rainfall and earthquakes decrease Fos by generating hydrostatic pressure H in
219 the vertical crack and horizontal seismic force E on the block.
220 A Cartesian coordinate system is established in three-dimensional space for the force analysis. The origin O is located at the
221 centre of the contact surface between sandstone and mudstone. For the case with two free surfaces, the orientation of the free
222 surfaces is set to be the positive direction of the x-axis and y-axis. For the case with three free surfaces, the negative direction
223 of the x-axis is also a free surface. Joint J2 is perpendicular to the x-axis, and joint J1 is perpendicular to the y-axis.
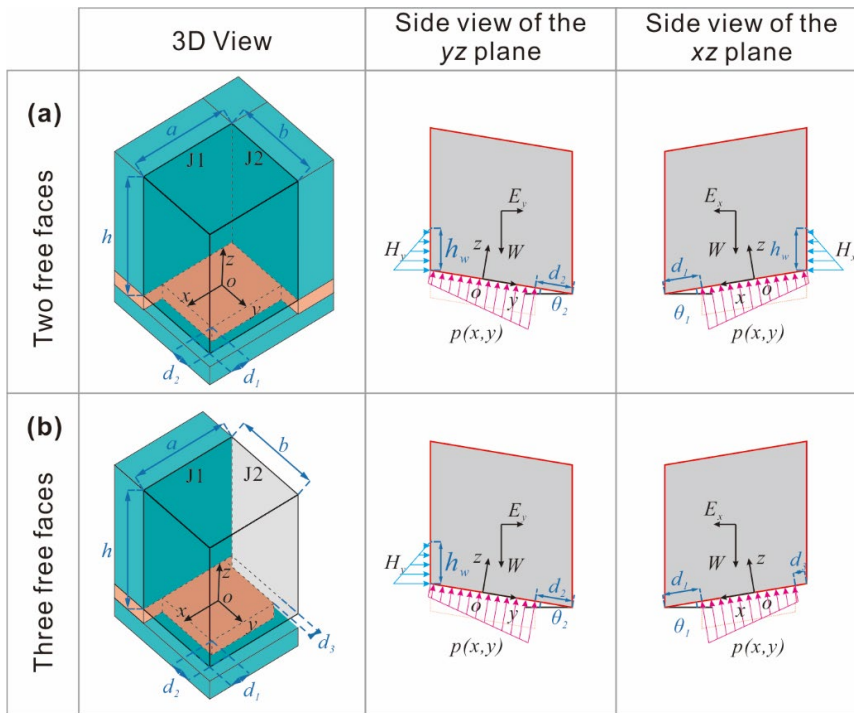
224

225 **Figure 8** Diagram of the force equilibrium analysis of the rock block model. (a) and (b) represent the case of unstable rock blocks with
226 two or three free vertical surfaces, respectively.

3.2 Calculation processes

3.2.1 Stress distribution at the block base

The following formulas are used to calculate the apparent dip of α (θ_1 and θ_2):

$$\theta_1 = \arctan(\tan\alpha \cdot \cos\omega_1) \tag{1}$$

$$\theta_2 = \arctan(\tan\alpha \cdot \cos\omega_2) \tag{2}$$

where ω_1 and ω_2 are the angles between the trend of the contact surface and the x direction or y direction, respectively.

As shown in Fig. 8b, with respect to the x-axis, gravity, seismic forces, and hydrostatic pressure create a non-symmetrical stress distribution on the foundation. The bending moment of gravity with respect to the x-axis (M_{bWx}) is

$$M_{bWx} = W \cdot \frac{d_1 - d_3}{2}\cos\theta_1 \tag{3}$$

Assuming that the height of the water in the fracture is h_w, the hydrostatic pressure along the x direction (H_x) and its bending moment (M_{bHx}) are respectively expressed as

$$H_x = \frac{\gamma_w h_w^2}{2}(b - d_2) \tag{4}$$

$$M_{bHx} = \int_{-\frac{b-d_2}{2}}^{\frac{b-d_2}{2}} \int_0^{h_w \cos\theta_1} \gamma_w \left(h_w - \frac{z}{\cos\theta_1}\right)\left(\frac{z}{\cos\theta_1} + \frac{a - d_1 - d_3}{2} \cdot \sin\theta_1\right) dz\,dy \tag{5}$$

The horizontal seismic force along x direction (E_x) and its bending moment (M_{bEx}) are respectively expressed as

$$E_x = k_e W \tag{6}$$

$$M_{bEx} = E_x \left(\frac{h}{2} - \frac{d_1 - d_3}{2}\sin\theta_1\right) \tag{7}$$

The total applied vertical load (N_z) and the total bending moments along the x direction (M_{bx}) can be derived as

$$N_z = W\cos\alpha - (H_x \cdot k_1 \cdot k_3 + E_x \cdot k_2)\sin\theta_1 - (H_y \cdot k_1 + E_y \cdot k_2)\sin\theta_1 \tag{8}$$

$$M_{bx} = M_{bWx} + M_{bHx} \cdot k_1 \cdot k_3 + M_{bEx} \cdot k_2 \tag{9}$$

where k_1, k_2 and k_3 are the coefficients set to make Eq. (8) and Eq. (9) compatible with different calculation scenarios. Therefore, Eqs. (8) and (9) and the following formulas can be expressed in a unified form. In the natural scenario, k_1 and k_2 are both equal to 0. In the rainfall scenario, $k_1 = 1$. In the earthquake scenario, $k_2 = 1$. For the case of two free faces, $k_3 = 1$. For the case of three free surfaces, $k_3 = 0$.

Based on bending theory (Adrian, 2010), the eccentricity distance along the x direction (e_x) can be expressed as

$$e_x = \frac{M_{bx}}{N_z} = \frac{M_{bWx} + M_{bHx} \cdot k_1 \cdot k_3 + M_{bEx} \cdot k_2}{W\cos\alpha - (H_x \cdot k_1 \cdot k_3 + E_x \cdot k_2)\sin\theta_1 - (H_y \cdot k_1 + E_y \cdot k_2)\sin\theta_1} \tag{10}$$

The same method can be used to obtain e_y:

$$e_y = \frac{M_{by}}{N_z} = \frac{M_{bWy} + M_{bHy} \cdot k_1 + M_{bEy} \cdot k_2}{W\cos\alpha - (H_x \cdot k_1 \cdot k_3 + E_x \cdot k_2)\sin\theta_1 - (H_y \cdot k_1 + E_y \cdot k_2)\sin\theta_1} \tag{11}$$

254 According to the stress distribution of a rectangular shaped foundation ([Adrian, 2010](#)), the stress in the (x, y) coordinates,

255 $p(x, y)$, is

$$p(x, y) = \frac{N}{A} + \frac{Ne_x}{I_y}x + \frac{Ne_y}{I_x}y \tag{12}$$

257 with the formulas

$$I_x = \frac{(a - d_1)(b - d_2)^3}{12} \tag{13}$$

$$I_y = \frac{(b - d_2)(a - d_1)^3}{12} \tag{14}$$

$$A = (a - d_1 - d_3)(b - d_2) \tag{15}$$

261 By substituting Eq. (13-15) into Eq. (12), $p(x, y)$ can be derived as

$$p(x, y) = \frac{N}{A}\left[1 + \frac{12e_x}{(a - d_1 - d_3)^2}x + \frac{12e_y}{(b - d_2)^2}y\right] \quad x \in \left[-\frac{a - d_1 - d_3}{2}, \frac{a - d_1 - d_3}{2}\right], y \in \left[-\frac{b - d_2}{2}, \frac{b - d_2}{2}\right] \tag{16}$$

263 p_{max} and p_{mim} can be derived from Eq. (16) as

$$p_{max} = p\left(\frac{a - d_1 - d_3}{2}, \frac{b - d_2}{2}\right) \tag{17}$$

$$p_{min} = p\left(-\frac{a - d_1 - d_3}{2}, -\frac{b - d_2}{2}\right) \tag{18}$$

266 The mudstone foundation has both compressive strength and tensile strength, so the value of $p(x, y)$ is modified to obtain the

267 two piecewise functions

$$p_p(x, y) = \begin{cases} \sigma_{cmax}, & p(x, y) \geq \sigma_{cmax} \\ p(x, y), & 0 < p(x, y) \leq \sigma_{cmax} \\ 0, & p(x, y) < 0 \end{cases} \tag{19}$$

$$p_n(x, y) = \begin{cases} 0, & p(x, y) < -\sigma_{tmax} \\ p(x, y), & -\sigma_{tmax} \leq p(x, y) < 0 \\ 0, & p(x, y) \geq 0 \end{cases} \tag{20}$$

270 Here, $p_p(x, y)$ provides support normal force for the overhanging sandstone, and $p_n(x, y)$ provides tension force.

271 **3.2.2 Calculation of factors of safety**

272 According to the Mohr-Coulomb criterion, the ultimate shear strength τ_{max} is

$$\tau_{max} = \int_{-\frac{a-d_1-d_3}{2}}^{\frac{a-d_1-d_3}{2}} \int_{-\frac{b-d_2}{2}}^{\frac{b-d_2}{2}} \left[p_p(x, y)\tan\varphi + c\right]dy\,dx \tag{21}$$

274 Therefore, Fos against sliding, Fos_{sl}, can be defined as

$$Fos_{sl} = \frac{S_{stabilizing}}{S_{sliding}} = \frac{\tau_{max}}{W|\sin\alpha_s| + H_x \cdot \cos\omega_s \cdot \cos\alpha_s \cdot k_1 \cdot k_3 + H_y \cdot |\sin\omega_s| \cdot \cos\alpha_s \cdot k_1 + E \cdot \cos\alpha_s \cdot k_2} \tag{22}$$

276 When the block can slide freely, $\alpha_s = \alpha$, $\omega_s = 0$; when the block is constrained to slide along a joint plane (e.g., J1), $\alpha_s =$

277 θ_1 or θ_2, $\omega_s = \omega_1$ or ω_2. For the case of an anaclinal slope, the sliding direction is opposite to the free surface. Therefore, the

278 rock block does not slide, and Fos_{sl} is not considered in the model.

279 With regard to stability against toppling, along the x direction, the part of the block above the mudstone base provides the

280 stabilizing moment $M_{W_{inx}}$, and the part of the block above the basal cavity provides the overturning moment $M_{W_{outx}}$. When

281 tension exists, there is an additional stabilizing moment. M_{px}, $M_{W_{inx}}$, $M_{W_{outx}}$ and M_{px} can be derived as

$$M_{W_{inx}} = W\frac{a - d_1}{a}\cos\theta_1 \cdot \left(\frac{a - d_1}{2}\right) \tag{23}$$

$$M_{W_{outx}} = W\frac{d_1}{a}\cos\theta_1 \cdot \frac{d_1}{2} \tag{24}$$

$$M_{px} = -\int_{-\frac{b-d_2}{2}}^{\frac{b-d_2}{2}}\int_{-\frac{a-d_1-d_3}{2}}^{\frac{a-d_1-d_3}{2}} p_n(x,y) \cdot \left(\frac{a}{2} - d_1 - x\right) dx\, dy \tag{25}$$

285 and M_{Hx} and M_{Ex} can be derived as

$$M_{Hx} = \int_{-\frac{b-d_2}{2}}^{\frac{b-d_2}{2}}\int_0^{h_w\cos\theta_1} \gamma_w\left(h_w - \frac{z}{\cos\theta_1}\right)\left(\frac{z}{\cos\theta_1} + (a - d_1)\sin\theta_1\right) dz\, dy \tag{26}$$

$$M_{Ex} = E_x\left(\frac{h}{2} + \left(\frac{a}{2} - d_1\right)\sin\theta_1\right) \tag{27}$$

288 Therefore, the Fos against toppling along the x direction, Fos_{tox}, results in

$$Fos_{tox} = \frac{M_{stabilizing}}{M_{overturning}} = \frac{M_{W_{inx}} + M_{px}}{M_{W_{outx}} + M_{Hx} \cdot k_1 \cdot k_3 + M_{Ex} \cdot k_2} \tag{28}$$

290 Similarly, Fos_{toy} can be obtained as

$$Fos_{toy} = \frac{M_{stabilizing}}{M_{overturning}} = \frac{M_{W_{iny}} + M_{py}}{M_{W_{outy}} + M_{Hy} \cdot k_1 + M_{Ey} \cdot k_2} \tag{29}$$

292 The smaller value is selected as the Fos of the toppling failure mode Fos_{to}:

$$Fos_{to} = min\left(Fos_{tox}, Fos_{toy}\right) \tag{30}$$

294 When the stress on mudstone exceeds its strength, it causes partial damage and decreases the stability of the rock block.

295 Therefore, Fos with the consideration of compressive strength (Fos_{co}) and tensional strength (Fos_{te}) can be derived as

$$Fos_{co} = \frac{\sigma_{cmax}}{p_{max}} \tag{31}$$

$$Fos_{te} = \frac{\sigma_{tmax}}{-p_{min}} \tag{32}$$

298 Fos_{co} and Fos_{te} represent the current damage degree of mudstone due to compressive stress and tensile stress, respectively.

299 When the stress exceeds the ultimate strength, the strength of the mudstone is reduced to the residual value, and the initial

300 deformation appears. The ability of mudstone to provide resistance to the sliding and toppling of sandstone blocks is thus

301   reduced, and Fos_{sl} and Fos_{to} subsequently decline. The smaller the value of Fos_{co} and Fos_{te}, the greater the damage to the

302   underlying mudstone. The effective contact area between sandstone and mudstone becomes smaller as the development of

303   compressive and tension damage, which significantly affects the stability of the overhanging sandstone block.

304   Summarizing, four Fos of unstable rock block are obtained. Fos_{sl} and Fos_{to} are routine indicators directly representing the

305   stability of sandstone blocks. Fos_{co} and Fos_{te} are two indicators proposed in this study for the stability analysis of biased

306   rockfall, which describe the damage state of the underlying mudstone base. It is necessary to simultaneously consider four Fos

307   to evaluate the stability of unstable biased rockfall. The entire calculation process is shown in Fig. 9.

308
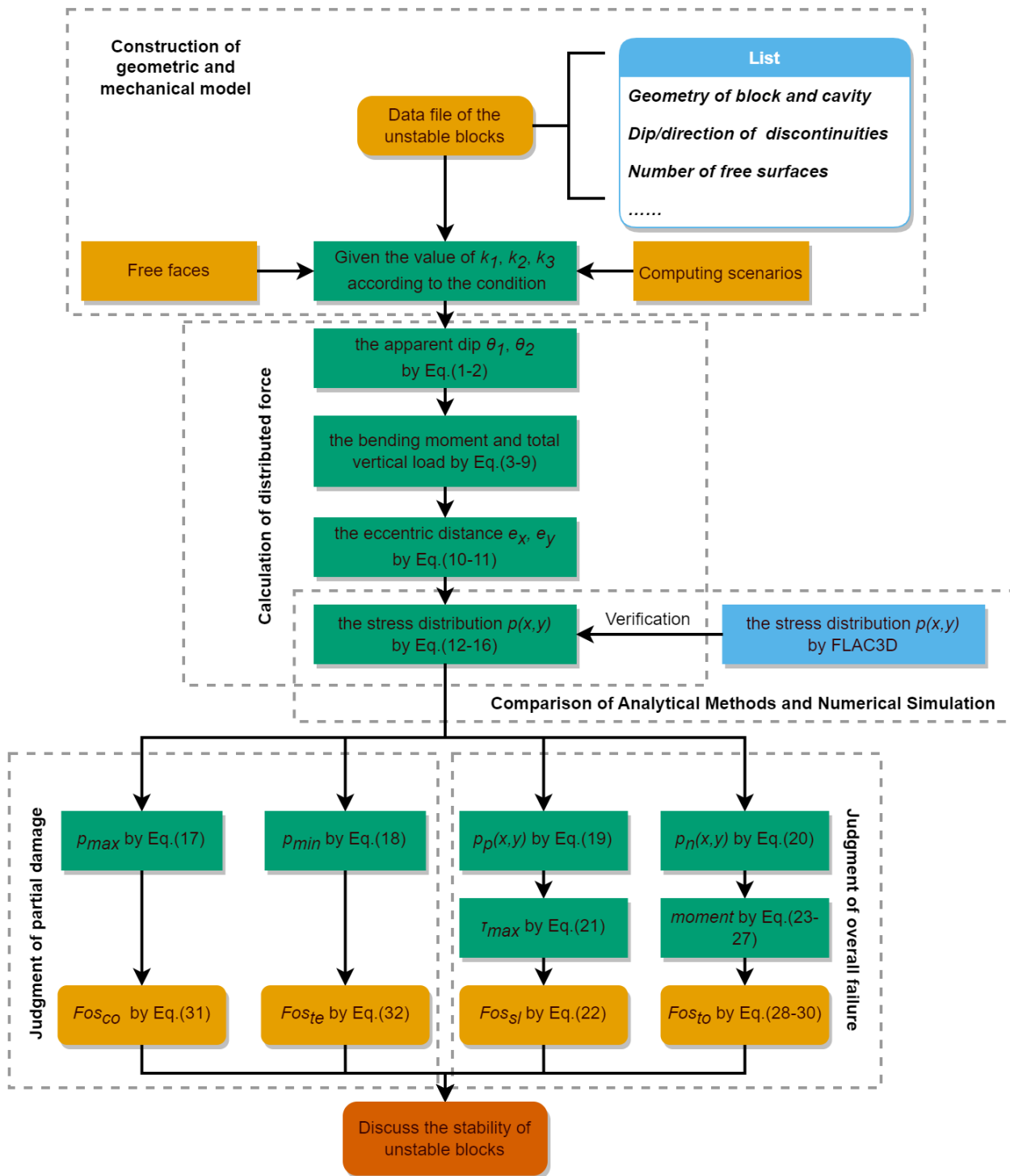
309

310   **Figure 9** Calculation process of Fos of the unstable rock blocks.

4 Validation of analytical methods by numerical simulation

The damage mechanisms at the base of the rock block play an important role in the rockfall evolution process. However, the stress distribution on the contact surface calculated by the proposed analytical methods is difficult to be validated by the field data. Therefore, numerical simulation of a biased rockfall was conducted in this study to determine the stress distribution on the contact surface between overhanging sandstone and underlying mudstone. Numerical simulations can take into account material deformation which is a drawback of the analytical methods. FLAC3D, a professional software that utilizes the finite difference method (FDM) for three-dimensional analysis of rocks, soils, and other materials, was employed for the 3D numerical simulation. Based on the geological models, a 3D numerical simulation model was conducted with FLAC3D 6.00 to analyse the stress distribution on the contact surface (Fig. 10).
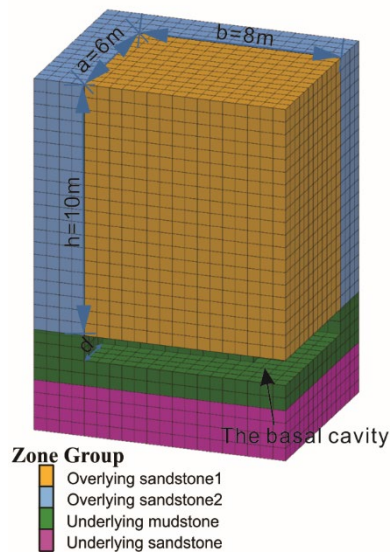
Figure 10 Numerical model built in FLAC3D.

The model is mainly composed of sandstone and mudstone, which the Overhanging sandstone1 represents an unstable rock block (dimensions a×b×h are 6 m, 8 m, 10 m respectively), and the weathering process of the mudstone is represented by excavating in stages in the underlying mudstone. Considering the deformation of the materials, sandstone was considered as elastic model, and mudstone was assigned Mohr-Coulomb model. Material properties were determined by referring to published literature and investigation reports in the study area. The sandstone has a unit weight (γ_s) 25 kN/m^3, an elastic modulu of 4530 Mpa and a Poisson's ratio of 0.183(Tang et al., 2010), and the mudstone has a unit weight 22.54 kN/m^3, an elastic modulu of 587 Mpa and a Poisson's ratio of 0.232. The friction angle of the contact surface (φ) is set to 25° and the cohesion (c) is set to 70 kPa (Zhang et al., 2016). Because of the strength degradation of mudstone foundations due to intense weathering, the maximum compressive stress of mudstone (σ_{cmax}) is replaced by the bearing capacity of mudstone foundations (2300 kPa), which is obtained through plate load tests in adjacent areas (Zheng et al., 2021). In addition, the

maximum tensile stress of mudstone (σ_{tmax}) is valued as one-ninth of σ_{cmax}. The west, north and bottom boundaries of the model are constrained by roller boundary conditions. The cohesion and internal friction angle of the interface between Overhanging sandstone1 and Overhanging sandstone2 are set to 0. After reaching the initial force-equilibrium state, the mudstone was excavated to simulate the weathering process, and the vertical stress distribution on the sand-mudstone interface at different basal cavity depths was obtained, as shown in Figure 11.
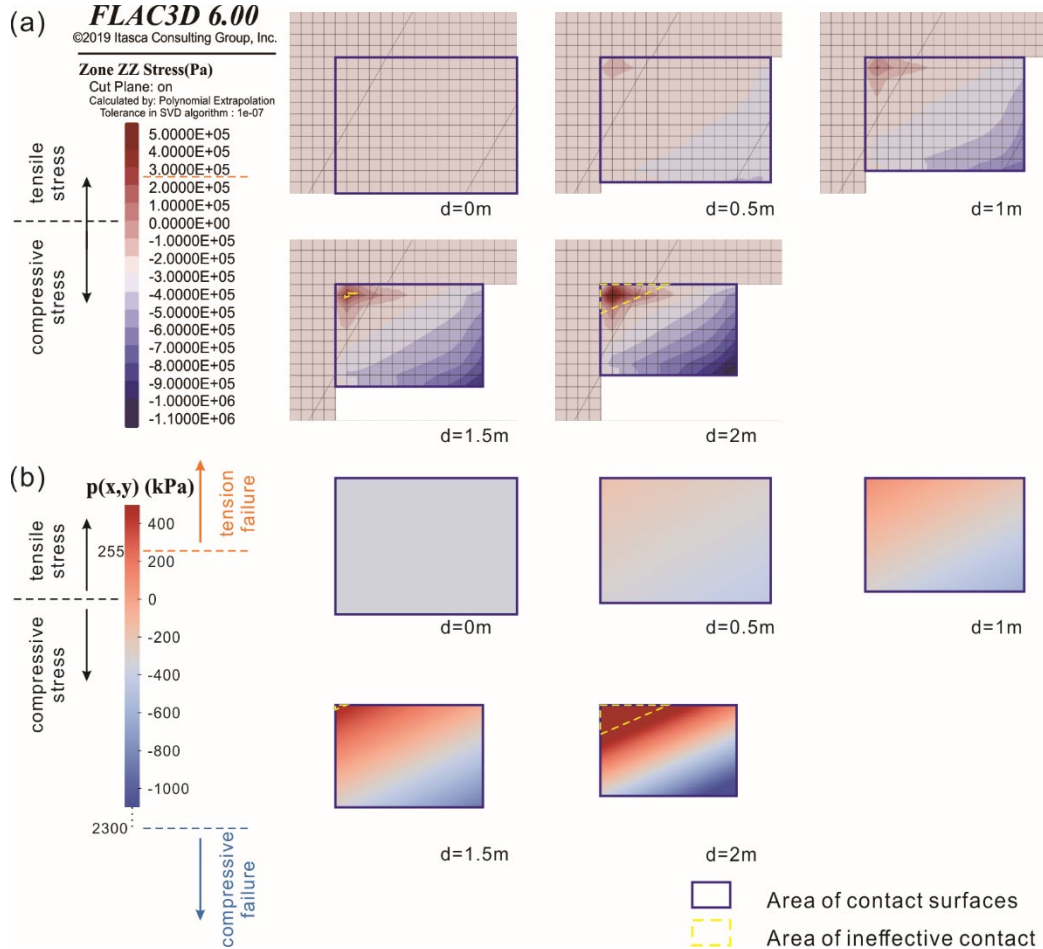
Figure 11 Diagram of stress distribution in the vertical direction on the contact interface through different methods, (a) the results of numerical simulation by FLAC3D, (b) the results of proposed analytical method.

When there is no cavity present, represented by d= 0 m, the stress distribution is uniform compressive stress (According to the FLAC3D software, compressive stresses are negative). At d=0.5 m, the stress remains entirely compressive, but non-uniform stress distribution occurs on the contact surfaces. At d=1 m, the vertical stress value in the upper left corner of the contact interface surpasses 0 (Fig.11), indicating the presence of tensile stress. As d increases to 1.5 m or 2 m, the tensile stress in the upper left corner gradually intensifies, exacerbating the non-uniform stress distribution. The results obtained from the

347 numerical simulation align with those from the analytical method, confirming the existence of tensile stress at the contact

348 interface in the biased rockfall due to external erosion development (Fig.11). Tensile stress commonly emerges within the

349 contact surface, making it challenging to observe directly in the field.

350 In the context of the limit equilibrium method, the contact area plays a vital role in stability analysis, as shown in Eq. (21)-(30)

351 in Section 3. The numerical simulation process provides an intuitive understanding of the influence of non-uniform stress

352 distribution on the contact surfaces on the stability of rock blocks. Whether subjected to tension or compression, the rock layer

353 has an ultimate strength. In Fig.11, when d=1.5 m or 2 m, the tensile stress exceeds the ultimate tensile strength, leading to

354 tensile failure in the upper left corner of the stress distribution diagram. The region enclosed by a yellow dotted line represents

355 ineffective contact, where no anti-slip force or overturning moment can be generated due to tension failure at the contact

356 surface. Therefore, this area needs to be subtracted from the total contact area when calculating Fos_{sl} and Fos_{to}. Similar

357 situations occur when the compressive stress exceeds the ultimate compressive strength. The current maximum compressive

358 stress has not reached the ultimate compressive strength in Figure 11. However, as d continues to increase, the area of

359 compression failure will appear in the lower right corner of diagram in Figure 11. This occurrence diminishes the area capable

360 of providing anti-slip force or overturning moment, thereby reducing the stability of the rock blocks.

361 The traditional LEM method does not account for distributed forces and fails to consider changes in the contact surface. The

362 method proposed in this study addresses this issue and is applied to the calculation of the Fos_{sl} and Fos_{to} as presented in Eq.

363 (21), (25) and (26).

5 Results

365 A detailed field investigation was carried out in the source area of rockfall (Fig. 3d). The size of the blocks was determined by

366 on-site measurement with tape and a laser rangefinder. The external erosion in mudstone were measured with a steel ruler, and

367 the morphological characteristics of mudstone foundation were mainly described with the average erosion depth of the basal

368 cavity. The attitude of discontinuities was measured by compass. The mechanical parameters have been given in Section.4.

369 The height of the water level (h_w) is set to be one-third of h, and an earthquake contribution coefficient k_e of 0.05 is considered

370 in stability calculations. The data obtained from the field survey were organized according to the coordinate system of the

371 geological model in Section 3.1, and Fos was calculated according to the calculation steps in Section 3.2. The calculated

372 geometric parameters and Fos results are shown in Table 2.

Table 2 Geometric parameters of rock blocks in the study area and *Fos* results.

Block number	Free faces	h [m]	a [m]	b [m]	d₁ [m]	d₂ [m]	d₃ [m]	α [°]	BD	J1	J2	Fos_{te}	Fos_{co}	Fos_{sl}	Fos_{to}	Fos_{min}	Fos_{te}	Fos_{co}	Fos_{sl}	Fos_{to}	Fos_{te}	Fos_{co}	Fos_{sl}	Fos_{to}
									Dip direction [°]			NS (Natural scenario)					RS (Rainfall scenario)				ES (Earthquake scenario)			
W01	3	23	7.2	6.1	0.65	0.25	0.17	6	78	7	97	-	2.99	5.61	101.54	2.99	-	2.56	3.18	11.91	0.90	1.63	3.81	4.88
W02	3	23	6.42	5.25	0.78	0.4	0.31	16	148	51	141	-	2.84	2.10	52.28	2.10	-	2.33	1.54	8.49	0.51	1.48	1.82	3.79
W03	2	20	3.5	2.6	0.84	0.55	-	7	341	53	143	0.52	1.56	16.53	4.72	0.52	0.15	0.86	2.83	1.02	0.14	0.81	9.12	1.01
W04	2	19	4.6	4.6	0.62	0.77	-	7	273	65	155	7.35	2.37	-	24.74	2.37	0.80	1.81	-	6.83	0.35	1.38	-	3.23
W05	2	15	16.7	5.6	2.13	1.36	-	5	283	50	140	1.70	2.57	-	9.86	1.70	1.19	2.39	-	6.10	0.63	1.99	-	3.36
W06	3	20	16.7	9.7	7.5	4.2	3.9	5	302	226	316	0.15	0.87	8.67	1.53	0.15	0.15	0.84	4.73	1.52	0.12	0.72	5.96	1.16
W07	2	22	9.2	3.7	0.64	0.8	-	12	324	315	405	-	2.27	2.82	22.86	2.27	0.57	1.55	1.62	2.97	0.34	1.28	2.44	2.21
W08	2	23	12	7.9	2	1.9	-	3	317	332	422	0.76	1.55	11.75	8.99	0.76	0.51	1.40	4.51	5.09	0.29	1.14	6.29	2.84
W09	2	18	8.4	6	0.9	2.5	-	8	60	335	425	0.38	1.48	4.98	2.23	0.38	0.29	1.30	2.87	1.56	0.22	1.12	4.08	1.20
W10	2	23	5.7	3.3	1.3	0.85	-	5	329	313	403	0.30	1.16	7.41	2.53	0.30	0.12	0.71	2.30	0.71	0.11	0.68	5.84	0.75
W11	3	22	1.1	2	0.1	0.64	0.1	4	327	120	210	1.13	1.74	19.08	4.97	1.13	0.12	0.69	2.37	0.51	0.07	0.49	10.57	0.73
W12	2	25	3.9	4	0.74	0.96	-	12	355	297	387	0.64	1.44	2.78	10.36	0.64	0.15	0.82	1.48	1.81	0.14	0.75	2.70	1.61
W13	2	12	11.9	10.9	3	2.28	-	7	36	73	163	1.06	2.77	7.28	9.39	1.06	0.99	2.71	5.63	9.02	0.70	2.41	4.93	5.65
W14	3	19	13	5	0	1.1	0	8	296	73	163	-	2.67	6.40	12.57	2.67	3.75	2.28	3.09	5.15	0.68	1.75	4.41	2.94
W15	2	18	22	6	8.3	0	-	8	351	200	290	0.70	1.84	9.74	2.93	0.70	0.60	1.75	5.03	2.83	0.39	1.50	5.79	2.34
W16	3	11	5.2	7.6	0	2.9	0	13	42	144	234	1.09	3.04	3.46	3.65	1.09	1.01	2.96	2.84	3.45	0.62	2.45	2.98	2.45
W17	3	7	8	2	0	0.56	0	20	30	156	246	7.71	6.72	3.07	6.83	3.07	3.40	5.87	2.29	4.49	1.48	4.70	2.81	2.86
W18	2	12	8.5	4.5	1.61	1.27	-	2	252	253	343	0.97	2.66	20.49	7.05	0.97	0.75	2.46	10.06	4.50	0.50	2.08	8.90	2.82
W19	2	15	4.2	5.2	1.6	0.68	-	5	28	56	146	0.75	2.12	8.71	5.49	0.75	0.48	1.80	4.17	3.66	0.31	1.48	5.79	2.24
W20	3	15	1.8	1.7	0.23	0.5	0.3	4	20	63	153	7.96	2.95	9.44	6.08	2.95	0.29	1.43	3.39	0.87	0.18	1.07	7.12	1.03
W21	3	20	18.9	9	0	2	0	7	348	71	161	-	2.51	4.96	12.25	2.51	-	2.36	3.31	7.48	1.15	1.90	3.58	3.95
W22	2	7	5.4	5.7	1	1.65	-	6	294	53	143	1.53	4.48	-	5.78	1.53	1.44	4.38	-	5.37	1.00	3.81	-	3.88

Note: When there is no tensile stress in the mudstone foundation, Fos_{te} has no value. For the case of an anaclinal slope, blocks do not slide and Fos_{sl} has no value. Both parameters are replaced by "-".

6 Discussion

6.1 Characteristics of rock block stability

There are up to 12 results of Fos per potential unstable block with the consideration of three scenarios and four failure modes (i.e., partial damage and overall failure). Most Fos_{te} values are less than 1 in all scenarios (yellow points in Fig.12), except for two blocks (i.e., W17 and W20), whose Fos_{te} values are also close to 1 under rainfall or earthquake scenarios. Although most of Fos_{co} values (green points in Fig. 12) are greater than 1, they are closer to the critical state of $Fos = 1$ than Fos_{sl} and Fos_{to} (represented by blue and orange points in Fig. 12, respectively). The compression damage of the exposed mudstone can be investigated in the field survey (Fig. 4d). However, it is difficult to observe the phenomenon of tensile damage inside the mudstone base. In the case of weak tensile strength, the mudstone base suffers from tensile failure, and compression failure usually occurs before tension failure. According to the results, their Fos_{te} and Fos_{co} are less than 1 or close to 1, which means that the underlying mudstone has been partially damaged due to slight compressive or tensile failure, and the blocks are potentially unstable with the current depth of the basal cavity. However, most of the blocks do not exhibit overall failure, and they still exist on the slope. Moreover, their Fos_{sl} and Fos_{to} values are greater than 1 in different scenarios, which is consistent with this actuality. The results indicate that most of the blocks are close to a critical state, in which they are partially damaged but the whole block is still stable.
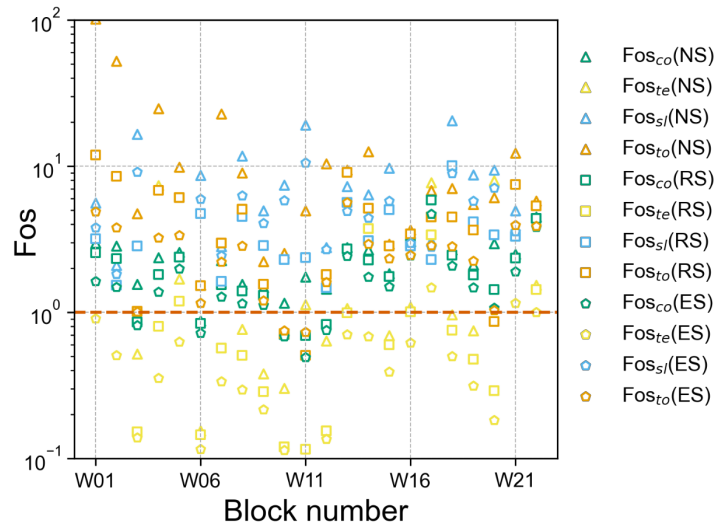
Figure 12 Distribution of Fos in different scenarios. Shapes represent different scenarios and colours represent different failure modes.

6.2 Relationship between Fos and geometric parameters

Fig. 13 presents the relationship between Fos_{min} and two main geometric parameters, the dip of the contact surface and the retreat ratio. In general, the dip angle of the contact surface (α) is the key factor influencing the sliding failure mode. The

394   horizontal axis in Fig. 13a is α between the rock blocks and underlying mudstone. Most of the points in Fig. 13a are in the
395   interval [0, 8°], which is consistent with the features of sub-horizontal strata in the study area. The shade of the points does not
396   change significantly in the x-axis direction, as Fig. 13a shows. Therefore, compared with the maximum retreat ratio (r_{max}),
397   the dip of the contact surface has less influence on rockfall stability in the study area. There was a significant positive
398   correlation between the retreat ratio (r_{max}) and Fos_{min}. In Fig. 13b, as the retreat ratios increase in the positive direction of
399   the x-axis and y-axis, the rock blocks show a notable tendency to be unstable.
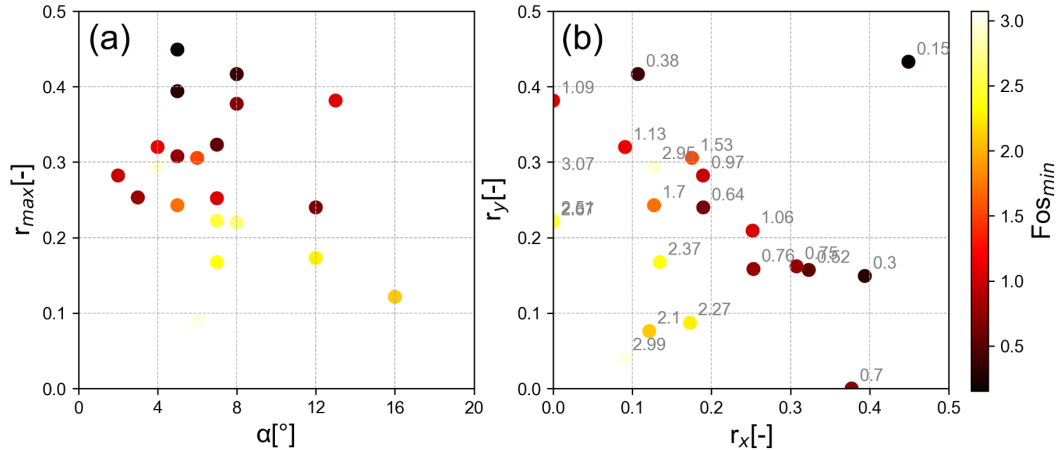
400

401   **Figure 13** Correlation between Fos and the dip of contact surface and retreat ratio. Here, α is the dip angle of the contact surface between
402   rock block and underlaying mudstone, r_x and r_y are the retreat ratio along x direction and y direction, respectively, equal to d_1/a and d_2/b,
403   and r_{max} is the larger of r_x and r_y.

404   **6.3 Definition of rockfall susceptibility**

405   To explore the variation in Fos with the progressive erosion process of the mudstone on the blocks, the mudstone retreat
406   velocities in different directions are assumed to be equal (5 mm/year, Zhang et al. (2016)). Fig. 14 shows the variations in Fos
407   of two specific blocks during the evolution process of the basal erosion in the mudstone. In the initial stage, the basal cavity is
408   small, and the overhanging block is stable; all Fos values are greater than 1.0. The basal cavity expands over time as the
409   mudstone weathers; then, the contact area decreases, and non-uniform distributed stress arises. When the stress exceeds the
410   ultimate strength of mudstone in a partial area, Fos_{co} and Fos_{te} decrease significantly, as shown in Fig. 14. The instability of
411   the blocks starts from the failure (or damage) of the foundation. Fos_{te} and Fos_{co} reach the critical state much earlier than
412   Fos_{sl} and Fos_{to}. For these two specific blocks, when r_{max} increases to 0.4, Fos_{sl} and Fos_{to} are still higher than 1.0. This
413   means that the rock blocks can remain globally stable in this condition.

414   These results further elucidate the stability analysis model proposed in this study. Fos_{co} and Fos_{te} introduced in this model
415   present the damage state of basal mudstone caused by compressive and tensile stresses, which do not provide global instability
416   of the overhanging block as sliding and toppling. However, Fos_{co} and Fos_{te} are important preliminary signs of subsequent

417 global failure of the rock block, as presented through the numerical simulation in Section 4. The damage in the basal mudstone

418 can significantly accelerate weathering and prompt expansion of the basal erosion, which will lead to global failure. The lower

419 Fos_{co} and Fos_{te} are, the lesser the safety margin of the blocks. Therefore, the four Fos used in this study can provide a more

420 comprehensive quantification of rockfall stability.

421 This result is consistent with Fig. 12, in which 63.7% of the yellow and green points (Fos_{te} and Fos_{co}) are located between

422 $Fos = 0.7$ and $Fos = 2.0$. This result can be validated by the field phenomena. In the study area, rock damage (e.g., micro-

423 fractures and cleavages) can be observed in the underlying mudstone. However, most overhanging rock blocks are stable at

424 the present time. This means that even if Fos_{sl} or Fos_{to} is higher than 1, its foundation has begun to be damaged. In the case

425 of heavy rain or earthquakes, Fos_{sl} and Fos_{to} may be reduced to less than 1, and the rockfall occurs.
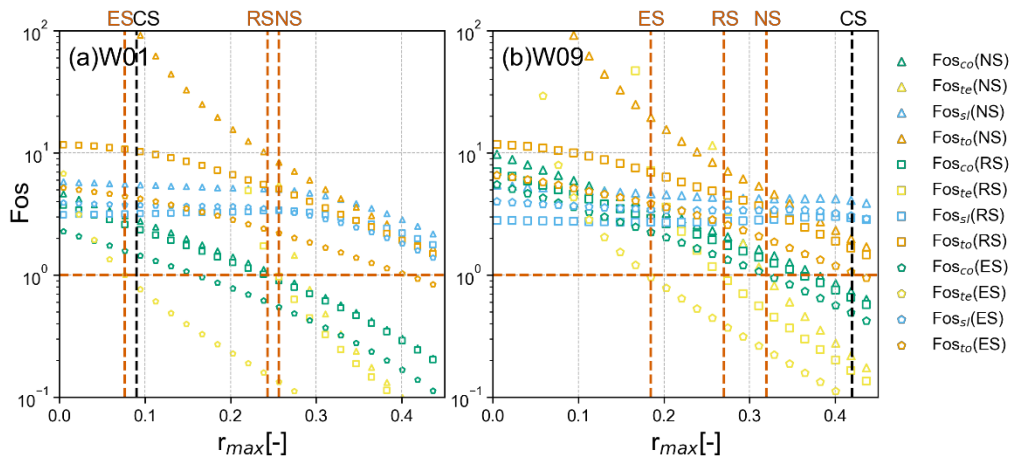
426

427 **Figure 14** Variation in Fos with r_{max}. (a) and (b) are the results for W01 and W09, respectively, which represent the situation of the blocks

428 with two and three free faces. The black dotted line (CS) approximately represents the current state of the unstable blocks. The red dotted

429 lines correspond to the critical values of r in different scenarios.

430

431 Based on the meaning of four Fos, rockfall susceptibility can be divided into three levels. When both Fos_{co} and Fos_{te} are

432 greater than 1, the overall rock block is stable, and the mudstone base is not damaged, which is defined as "low susceptibility"

433 and represented by the blue area in Fig. 15. With the development of basal erosion, when Fos_{co} or Fos_{te} is less than 1 and

434 Fos_{sl} and Fos_{to} are higher than 1, the base undergoes be damaged, and the overhanging sandstone blocks remain relatively

435 stable. This state is defined as "moderate susceptibility" and represented by the yellow area. When Fos_{sl} or Fos_{to} is less than

436 1 in some scenarios, the rock blocks are in a "high susceptibility" state, which means that rockfalls are highly likely to occur.

437 Fig. 15a indicates that along with the increase in the mudstone retreat ratio, the susceptibility of W01 and W09 changes from

438 low susceptibility to moderate susceptibility in the natural scenario. As Fig. 15b and c show, when rainfall or earthquake occurs,

439 Fos_{sl} or Fos_{to} of some blocks is less than 1, which means that some blocks have evolved to the state of high susceptibility

440 and the overall sandstone blocks are unstable.
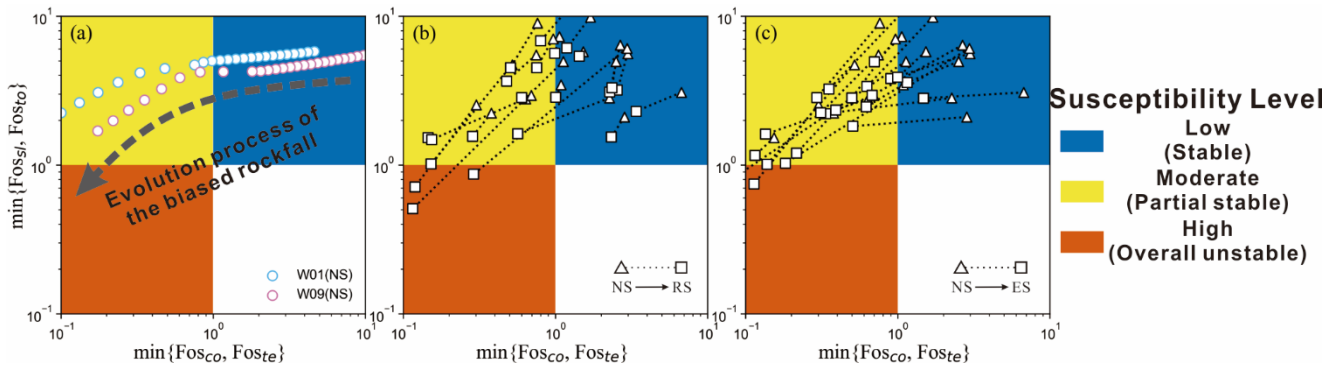
Figure 15 Rockfall susceptibility based on the combination of four Fos. The susceptibility is defined as three levels, represented by red, yellow and blue. (a) shows the progressive failure process of the rock block changing from low susceptibility to moderate susceptibility as the mudstone retreat ratio increases (illustrated by W01 and W09 in the natural scenario. (b) and (c) show the change in susceptibility of biased rock blocks, when the scenario changes from natural conditions to rainfall and earthquake conditions.

6.4 Critical retreat ratio in the study area

The basal erosion in the mudstone plays an important role in the progressive failure process of biased rockfall. To analyse the effect of the retreat ratio on the stability of rock blocks, all blocks in the study area were selected to calculate their Fos and susceptibility level with the increasing r, whose retreat velocities in different directions are assumed to be equal. Fig. 16 shows that along with the increase in the retreat ratio, the susceptibility level of rock blocks changes from low to moderate susceptibility. Corresponding to the critical state of min $\{Fos_{co}, Fos_{te}\} = 1$ of all blocks, the minimum retreat ratio is 0.26, and the maximum retreat ratio is 0.41, as marked by the vertical black dotted line in Fig. 16. According to the statistical analysis of critical retreat ratios, both mean and median are 0.33. Therefore, the critical retreat ratio of the rock blocks in the study area can be determined as 0.33, which is marked by the vertical red dotted line in the Fig. 16. The critical retreat ratio calculated by this method can be used for the preliminary identification of potential unstable rock blocks in a specific area, which can help concentrate limited risk treatment resources on these priorities. It should be emphasized that the mechanical parameters and analysis scenarios significantly affect the critical value. Therefore, the elaborative risk control of a given rockfall should be arranged based on its specific parameters and analysis scenarios.
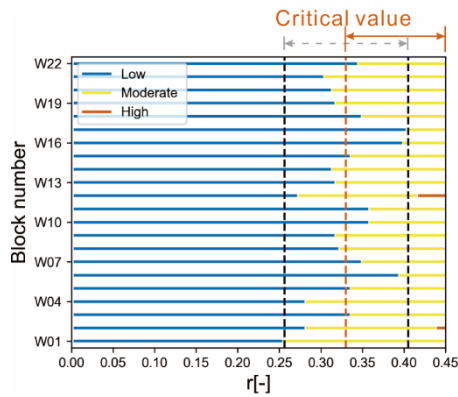
459

460 **Figure 16** Effect of the retreat ratio (r) on the Fos of the rock block, which is illustrated by all blocks in the study area.

461 **6.5 Limitations**

462 This study involves the development of an analytical model for the three-dimensional stability of biased rockfall, combining
463 the basic LEM method and the consideration of the non-uniform distribution. Due to the complexity of rock structure and force
464 analysis, it is necessary to highlight the limitations of this model.

465 First, this study uses a three-dimensional coordinate system and bending theory. It is difficult to consider diverse shapes of
466 rock blocks, and the rock block was simplified as a prismatic column. The assumption of fully persistent discontinuities may
467 underestimate the stability of rock blocks, and ignores the stress transmission in joints or rock bridges. Then, following the
468 basic framework of the general LEM method, this study assumed that the rock is not subjected to deformations. The complete
469 stress–strain behaviour, such as the deformation in the mudstone layer, is not considered in this study. The mode of tension
470 failure is very difficult to observe in the field, and it is currently verified by means of numerical simulation. Furthermore, the
471 block stability is strongly influenced by the uncertainty of mechanical parameters. However, because of the difficulties in
472 sampling strongly weathered mudstone, it is difficult to obtain adequate parameter values for uncertainty statistics. These
473 limitations will be important considerations in future studies.

474 **7 Conclusions**

475 Due to differential weathering in sub-horizontally interbedded of hard rock and soft rock, multi-layer biased rockfalls develop
476 on steep slopes. In mountainous ranges, cut slopes, and coastal cliffs, rockfall may cause significant facility damage and
477 casualties in residential areas and transport corridors. The aim of this study was to present a new three-dimensional analytical
478 method for the stability of rock blocks with basal cavities. In this method, a non-uniform distributed stress due to the
479 eccentricity effect is applied at the contact surface instead of a point force. The development of non-uniform distributed stress
480 calculated by the proposed analytical methods was validated by numerical simulation, which presents the evolution process of
481 biased rockfall from partial damage of the soft underlying layer, caused by non-uniform distributed stress, to toppling and

482 sliding of overhanging hard rock block due to overall unbalanced force. The method considers four failure modes according

483 to the rockfall evolution process, including partial damage of the soft foundation (Fos_{co} and Fos_{te}) and overall failure of the

484 rock block (Fos_{sl} and Fos_{to}).

485 Taking the northeast edge of the Sichuan Basin in Southwest China as the study area, the proposed method is used to calculate

486 the Fos of biased unstable rock blocks. The results show that in the natural scenario, the underlying mudstone of some rock

487 blocks has been partially damaged, and compression failure of the mudstone has been observed in the field. Some rock blocks

488 are expected to fail as a whole in rainfall or earthquake scenarios. The statistical analysis indicates that the retreat ratio is the

489 crucial factor influencing the Fos of biased rockfall. On the basis of different combinations of four Fos, rockfall susceptibility

490 was classified into three levels. As the retreat rate increases, the rock blocks undergo an evolution process from stability to

491 partial instability and then overall instability. Based on the current mechanical parameters of the eastern Sichuan Basin, the

492 critical retreat ratio from low to moderate rockfall susceptibility is 0.33.

493 The proposed method improves the three-dimensional mechanical model of a rock block with the basal erosion by considering

494 non-uniform distributed stress at the contact surface, which could promote the accuracy of rockfall stability analysis. Due to

495 the assumptions adopted and the complexity of the failure mechanism of biased rockfall, there are some limitations in this

496 method, mainly including the simplification of boundary conditions and rock deformation. These limitations will be important

497 considerations in future studies.

498 **Data availability**

499 All raw data can be provided by the corresponding authors upon request.

500 **Author contributions**

501 XS, BC and JD planned the campaign; XS and BC performed the field measurements; XS, BC, WW and BL designed and

502 developed the methodology. XS, BC and JD analysed the data; XS and BC wrote the manuscript draft; JD and WW reviewed

503 and edited the manuscript.

504 **Competing interests**

505 The authors declare that they have no conflicts of interest.

506 **Acknowledgements**

507 This research is funded by the National Natural Science Foundation of China (No. 42172318 and No. 42177159). The first

508 author thanks Master Chengjie Luo and Yu Wang for data collection in the field. We also appreciate the assistance of the

509   Research Center of Geohazard Monitoring and Warning in the Three Gorges Reservoir, China. We also thank the reviewers

510   for their suggestions that improved the quality of this paper.

References

512   Adrian, I.: Pressures distribution for eccentrically loaded rectangular footings on elastic soils, Proceedings of the 2010

513   international conference on Mathematical models for engineering science, Tenerife, Spain, 213–216,

514   Alejano, L. R., Carranza-Torres, C., Giani, G. P., and Arzua, J.: Study of the stability against toppling of rock blocks with

515   rounded edges based on analytical and experimental approaches, Eng. Geol., 195, 172-184,

516   https://doi.org/10.1016/j.enggeo.2015.05.030, 2015.

517   Alejano, L. R., Ordóñez, C., Armesto, J., and Rivas, T.: Assessment of the instability hazard of a granite boulder, Nat. Hazards,

518   53, 77-95, https://doi.org/10.1007/s11069-009-9413-0, 2010.

519   Ashby, J.: Sliding and toppling modes of failure in models and jointed rock slopes, M.S. thesis, Imperial College London

520   University, London, 1971.

521   Bray, J. W. and Goodman, R. E.: The theory of base friction models, Int. J. Rock Mech. Min. Sci. Geomech. Abstr., 18, 453-

522   468, https://doi.org/10.1016/0148-9062(81)90510-6, 1981.

523   Budetta, P.: Assessment of rockfall risk along roads, Nat. Hazards Earth Syst. Sci., 4, 71-81, https://doi.org/10.5194/nhess-4-

524   71-2004, 2004.

525   Budetta, P. and Nappi, M.: Comparison between qualitative rockfall risk rating systems for a road affected by high traffic

526   intensity, Nat. Hazards Earth Syst. Sci., 13, 1643-1653, https://doi.org/10.5194/nhess-13-1643-2013, 2013.

527   Chau, K. T., Wong, R. H. C., Liu, J., and Lee, C. F.: Rockfall hazard analysis for Hong Kong based on rockfall inventory,

528   Rock Mech. Rock Eng., 36, 383-408, https://doi.org/10.1007/s00603-002-0035-z, 2003.

529   Chen, H. K. and Tang, H. M.: Stability analysis method of perilous rock in source of avalanche, J. Geol. Min. Res., 2, 60-67,

530   https://doi.org/10.5897/JGMR.9000070, 2010.

531   Chen, H. K., Xian, X. F., Tang, H. M., and Feng, Q. H.: A massive development mechanism and countermeasures for perilous

532   rocks in the Three Gorges Reservoir area of PR China: The example of the Taibaiyan cliff at Wanzhou, Journal of Chongqing

533   University, 31, 1178-1184, https://doi.org/10.11835/j.issn.1000-582X.2008.10.019, 2008.

534   Corominas, J., Mavrouli, O., and Ruiz-Carulla, R.: Magnitude and frequency relations: are there geological constraints to the

535   rockfall size?, Landslides, 15, 829-845, https://doi.org/10.1007/s10346-017-0910-z, 2018.

536   Cruden, D. M. and Varnes, J. D.: Landslide types and processes. Landslides: investigation and mitigation, transportation

537   research board (National Research Council), National Academy Press, Washington, DC, 1996.

538   D'Amato, J., Hantz, D., Guerin, A., Jaboyedoff, M., Baillet, L., and Mariscal, A.: Influence of meteorological factors on

539   rockfall occurrence in a middle mountain limestone cliff, Nat. Hazards Earth Syst. Sci., 16, 719-735,

540   https://doi.org/10.5194/nhess-16-719-2016, 2016.

541 Derron, M. H., Jaboyedoff, M., and Blikra, L. H.: Preliminary assessment of rockslide and rockfall hazards using a DEM
542 (Oppstadhornet, Norway), Nat. Hazards Earth Syst. Sci., 5, 285-292, https://doi.org/10.5194/nhess-5-285-2005, 2005.

543 Ferrari, F., Giacomini, A., and Thoeni, K.: Qualitative Rockfall Hazard Assessment: A Comprehensive Review of Current
544 Practices, Rock Mech. Rock Eng., 49, 2865-2922, https://doi.org/10.1007/s00603-016-0918-z, 2016.

545 Frattini, P., Crosta, G., Carrara, A., and Agliardi, F.: Assessment of rockfall susceptibility by integrating statistical and
546 physically-based approaches, Geomorphology, 94, 419-437, https://doi.org/10.1016/j.geomorph.2006.10.037, 2008.

547 Frayssines, M. and Hantz, D.: Modelling and back-analysing failures in steep limestone cliffs, Int. J. Rock Mech. Min. Sci.,
548 46, 1115-1123, https://doi.org/10.1016/j.ijrmms.2009.06.003, 2009.

549 Guzzetti, F., Reichenbach, P., and Wieczorek, G. F.: Rockfall hazard and risk assessment in the Yosemite Valley, California,
550 USA, Nat. Hazards Earth Syst. Sci., 3, 491-503, https://doi.org/10.5194/nhess-3-491-2003, 2003.

551 Hutchinson, J. N.: Field and laboratory studies of a fall in Upper Chalk cliffs at Joss Bay, Isle of Thanet, in: Stress-Strain
552 Behaviour of Soils, Proceedings of the Roscoe Memorial Symposium, Oxfordshire, 29-31 March 1971, 692-706, 1972.

553 Jaboyedoff, M., Baillifard, F., Philippossian, F., and Rouiller, J. D.: Assessing fracture occurrence using "weighted fracturing
554 density": a step towards estimating rock instability hazard, Nat. Hazards Earth Syst. Sci., 4, 83-93,
555 https://doi.org/10.5194/nhess-4-83-2004, 2004.

556 Jaboyedoff, M., Ben Hammouda, M., Derron, M.-H., Guérin, A., Hantz, D., and Noel, F.: The Rockfall Failure Hazard
557 Assessment: Summary and New Advances, in: Understanding and Reducing Landslide Disaster Risk: Volume 1 Sendai
558 Landslide Partnerships and Kyoto Landslide Commitment, edited by: Sassa, K., Mikoš, M., Sassa, S., Bobrowsky, P. T.,
559 Takara, K., and Dang, K., Springer International Publishing, Cham, 55-83, https://doi.org/10.1007/978-3-030-60196-6_3,
560 2021.

561 Kogure, T., Aoki, H., Maekado, A., Hirose, T., and Matsukura, Y.: Effect of the development of notches and tension cracks
562 on instability of limestone coastal cliffs in the Ryukyus, Japan, Geomorphology, 80, 236-244,
563 https://doi.org/10.1016/j.geomorph.2006.02.012, 2006.

564 Kromer, R., Lato, M., Hutchinson, D. J., Gauthier, D., and Edwards, T.: Managing rockfall risk through baseline monitoring
565 of precursors using a terrestrial laser scanner, Can. Geotech. J., 54, 953-967, https://doi.org/10.1139/cgj-2016-0178, 2017.

566 Lin, D. and Fairhurst, C.: Static analysis of the stability of three-dimensional blocky systems around excavations in rock, Int.
567 J. Rock Mech. Min. Sci. Geomech. Abstr., 25, 139-147, https://doi.org/https://doi.org/10.1016/0148-9062(88)92296-6, 1988.

568 Malamud, B. D., Turcotte, D. L., Guzzetti, F., and Reichenbach, P.: Landslide inventories and their statistical properties, Earth
569 Surf. Process. Landf., 29, 687-711, https://doi.org/10.1002/esp.1064, 2004.

570 Matasci, B., Stock, G. M., Jaboyedoff, M., Carrea, D., Collins, B. D., Guerin, A., Matasci, G., and Ravanel, L.: Assessing
571 rockfall susceptibility in steep and overhanging slopes using three-dimensional analysis of failure mechanisms, Landslides,
572 15, 859-878, https://doi.org/10.1007/s10346-017-0911-y, 2018.

573 Pérez-Rey, I., Muñiz-Menéndez, M., González, J., Vagnon, F., Walton, G., and Alejano, L. R.: Laboratory physical modelling
574 of block toppling instability by means of tilt tests, Eng. Geol., 282, 105994, https://doi.org/10.1016/j.enggeo.2021.105994,
575 2021.

576 Pierson, L. A., Davis, S. A., and Van Vickle, R.: Rockfall hazard rating system–implementation manual, Federal Highway
577 Administration (FHWA), Report FHWA—OR-EG-90-01, FHWA, US Department of Transportation, 80 pp., 1990.

578 Sagaseta, C.: On the Modes of Instability of a Rigid Block on an Inclined Plane, Rock Mech. Rock Eng., 19, 261-266,
579 https://doi.org/10.1007/Bf01039998, 1986.

580 Santi, P. M., Russell, C. P., Higgins, J. D., and Spriet, J. I.: Modification and statistical analysis of the Colorado Rockfall
581 Hazard Rating System, Eng. Geol., 104, 55-65, https://doi.org/10.1016/j.enggeo.2008.08.009, 2009.

582 Volkwein, A., Schellenberg, K., Labiouse, V., Agliardi, F., Berger, F., Bourrier, F., Dorren, L. K. A., Gerber, W., and
583 Jaboyedoff, M.: Rockfall characterisation and structural protection – a review, Nat. Hazards Earth Syst. Sci., 11, 2617-2651,
584 https://doi.org/10.5194/nhess-11-2617-2011, 2011.

585 Ward, D. J., Berlin, M. M., and Anderson, R. S.: Sediment dynamics below retreating cliffs, Earth Surf. Process. Landf., 36,
586 1023-1043, https://doi.org/10.1002/esp.2129, 2011.

587 Wu, L. Z., Zhang, L. M., Zhou, Y., Xu, Q., Yu, B., Liu, G. G., and Bai, L. Y.: Theoretical analysis and model test for rainfall-
588 induced shallow landslides in the red-bed area of Sichuan, Bull. Eng. Geol. Environ., 77, 1343-1353,
589 https://doi.org/10.1007/s10064-017-1126-0, 2018.

590 Yu, B., Ma, E., Cai, J., Xu, Q., Li, W., and Zheng, G.: A prediction model for rock planar slides with large displacement
591 triggered by heavy rainfall in the Red bed area, Southwest, China, Landslides, 18, 773-783, https://doi.org/10.1007/s10346-
592 020-01528-x, 2021.

593 Zhan, J., Yu, Z., Lv, Y., Peng, J., Song, S., and Yao, Z.: Rockfall Hazard Assessment in the Taihang Grand Canyon Scenic
594 Area Integrating Regional-Scale Identification of Potential Rockfall Sources, Remote Sens., 14, 3021,
595 https://doi.org/10.3390/rs14133021, 2022.

596 Zhang, K., Tan, P., Ma, G. W., and Cao, P.: Modeling of the progressive failure of an overhang slope subject to differential
597 weathering in Three Gorges Reservoir, China, Landslides, 13, 1303-1313, https://doi.org/10.1007/s10346-015-0672-4, 2016.

598 Zhang, M., Yin, Y. P., and Huang, B. L.: Mechanisms of rainfall-induced landslides in gently inclined red beds in the eastern
599 Sichuan Basin, SW China, Landslides, 12, 973-983, https://doi.org/10.1007/s10346-015-0611-4, 2015.

600 Zhou, C., Yin, K. L., Cao, Y., Ahmed, B., Li, Y. Y., Catani, F., and Pourghasemi, H. R.: Landslide susceptibility modeling
601 applying machine learning methods: A case study from Longju in the Three Gorges Reservoir area, China, Comput. Geosci.,
602 112, 23-37, https://doi.org/10.1016/j.cageo.2017.11.019, 2018.

603 Zhou, Y., Shi, S., Zhang, Y., Cai, Q., Liang, J., and Cheng, Y.: Stability of unstable rock in nearly-horizontal sandstone-
604 mudstone stratum due to enlarged rock-cell, Journal of Engineering Geology, 25, 1220-1229,
605 https://doi.org/10.13544/j.cnki.jeg.2017.05.006, 2017.

606